2026 IEEE International Conference on Robotics and Automation (ICRA 2026)
June 1-5, 2026. Vienna, Austria

# Enhancing Pose Estimation Stability and Accuracy for Fiducial Markers Using Transparent Cylinders

Hideyuki Tanaka[1] and Kunihiro Ogata[2]

*Abstract*— **Planar fiducial markers are widely used for 6-DoF pose estimation in robotics and augmented reality; however, conventional markers suffer from reduced orientation accuracy in near-frontal views, pose ambiguity, and limited depth accuracy. We previously addressed these issues using lenticular-based high-accuracy markers, but their fabrication required specialized optical components. This paper proposes a novel self-fabricable fiducial marker that achieves comparable accuracy using transparent cylindrical rods. By attaching simple black-and-white printed patterns to acrylic cylinders, we realize two optical elements: a cylindrical Lenticular Angle Gauge (c-LEAG), which provides continuous orientation information, and a cylindrical Flip Detection Pattern (c-FDP), which enables robust pose-inversion detection. We analytically derive the relationship between viewing direction and pattern displacement using geometric optics and show that the orientation response is approximately linear within $\pm 15^\circ$. Based on these components, we develop c-LentiMark, integrating conventional feature-based pose estimation with cylinder-based pose correction. Experiments using a precision rotation stage demonstrate a measurable orientation range of approximately -74° to +74° and a significant improvement in frontal-view accuracy, reducing orientation errors to about 0.4°. The proposed marker achieves high accuracy comparable to previous lenticular designs while allowing low-cost fabrication from widely available materials.**

## I. INTRODUCTION

A fiducial marker is a planar pattern that enables 3D pose (position and orientation) estimation within a camera coordinate system, using images captured by a monocular camera. Originally, fiducial markers were developed for camera registration in Augmented Reality (AR) [1], but their applications have expanded to robotics for tasks like calibration [2][3], manipulation [4][5], localization [6][7], and navigation [8][9]. From the perspective of AI safety [10][11], fiducial markers play a crucial role in enhancing system safety, reliability, and explainability.

Several types of fiducial markers, including ARToolKit [12], RUNE-Tag [13], AprilTag [14], ChromaTag [15], and ArUco [16], provide simple, reliable 6-DoF measurement methods. These conventional markers rely on feature extraction and solving the perspective-n-point (PnP) problem [17][18] to obtain a transformation matrix between camera and marker coordinates. However, their accuracy diminishes, especially for small markers or when viewed from a frontal perspective [19] – a common issue for traditional methods.

This work was supported by the Acquisition, Technology & Logistics Agency (ATLA), Ministry of Defense, Japan, under the Security Technology Research Promotion Program.

[1]Hideyuki Tanaka and [2]Kunihiro Ogata are with Research Institute on Human and Societal Augmentation, National Institute of Advanced Industrial Science and Technology, Kashiwa, Chiba, Japan. hideyuki-tanaka@aist.go.jp,ogata.kunihiro@aist.go.jp

To overcome this limitation, the authors introduced the high-accuracy marker "LentiMark" in 2012 [20] and have since developed several enhanced versions [21]-[26]. These markers utilize specialized optical components to capture highly accurate orientation data, achieving more than ten times the accuracy of conventional markers, with positional errors as low as 0.2% and orientation errors of 0.5°. However, these components required specialized manufacturing techniques, limiting their accessibility and increasing production costs.

To address these challenges, the authors devised a method that replicates the functionality of these optical components using a single type of transparent cylinder, simplifying fabrication. The new marker demonstrated stable, highly accurate pose estimation comparable to traditional high-accuracy markers.

In this paper, we first review related work and previous high-accuracy markers in Section II. Section III details the optical components based on this novel approach using transparent cylinders for pose visualization. Section IV introduces the markers and measurement algorithms, while Section V presents evaluation experiments. The results underscore the effectiveness and applicability of this approach in fields such as AR and robotics.

## II. RELATED WORK AND CHALLENGES

This section reviews previous research aimed at improving the accuracy of 3D pose measurements for small, planar markers, while addressing the challenges involved. As outlined in the Introduction, conventional markers face accuracy limitations due to their design principles. This makes it difficult to improve accuracy using traditional methods, which depend on image data derived from flat-surface patterns printed on paper. The solution lies in introducing mechanisms that react sensitively to orientation changes, modifying their appearance accordingly. The following subsections explore research that has adopted this approach.

### A. Utilization of Moiré Patterns

Moiré patterns, created by the interference of two periodic structures, change based on viewing angle when layered on a transparent thin plate such as glass. These changes offer highly sensitive orientation data for accurate pose estimation. Armstrong [27][28] and Qiu et al. [29] utilized this technique to achieve pose accuracy exceeding conventional markers by over 100 times.

Despite these advances, traditional moiré patterns face challenges due to their typically dark and low-contrast

appearance, necessitating active lighting for measurement. Practical implementations often require backlighting or retroreflective materials to illuminate the pattern. Additionally, the stripes generating the moiré pattern must be precisely printed using techniques like photolithography, with accurate alignment between the two layers, making the fabrication process difficult for non-specialists.

### B. Utilization of Lenses

Another approach involves using lenses to alter the marker appearance based on the viewing angle. Mohan et al.'s Bokode [30] uses a small lens to allow a camera focused at infinity to observe a data matrix code behind the lens. This setup enables high-accuracy pose estimation by analyzing how the visible area changes with the viewing angle. However, it too requires backlighting and is challenging to manufacture. Additionally, a separate defocused camera is necessary for observation, and the measurable pose range is limited to about $\pm 20^\circ$, classifying it as a different category of tool from the markers designed for 3D pose measurement in this study.

Schillebeeckx developed markers using lenticular lenses and microlens arrays, where patterns change based on the viewing angle, either through color shifts [31] or changes in black-and-white patterns [32]. This method achieved over 10 times the pose estimation accuracy of conventional markers through encoded data. However, like the previously discussed methods, the markers require precise pattern printing and alignment with the lens, making them difficult to manufacture. Their use with low-cost webcams from a distance is impractical, and like other technologies, these patterns are not easily interpretable by humans, limiting their applications to camera-computer systems.

### C. LentiMark Method

The issues with traditional markers for pose measurement can be summarized as follows:

1) **Decreased orientation accuracy from the front:** Accuracy decreases when observed from the front (within $\pm 15^\circ$ from the perpendicular), resulting in orientation errors of $2^\circ$ to $20^\circ$.
2) **Pose ambiguity:** The orientation may not be uniquely determined, especially when the marker is small in the image or the camera has a narrow field of view (high magnification). This phenomenon occurs not only from the front but also from other directions.
3) **Decreased depth position accuracy:** Depth position measurement is less accurate compared to lateral measurements, often resulting in errors greater than 1% of the measurement distance.

The author has been addressing these issues since 2010 and developed a high-accuracy fiducial marker, LentiMark, between 2012 and 2017, which solves (or significantly improves) all three major problems. As shown in Fig. 1, LentiMark consists of a traditional marker and is accompanied by two LEAGs (lenticular angle gauges), two FDPs (flip detection patterns), and four feature dots. These components

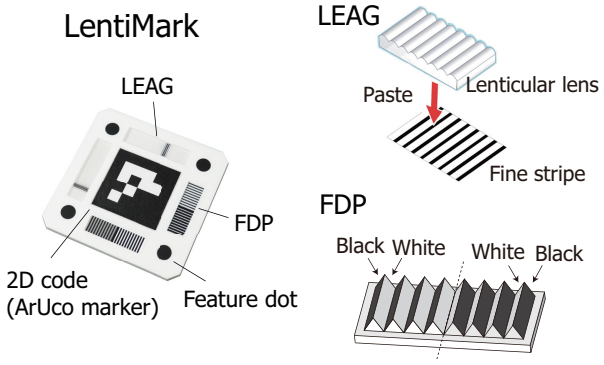


Fig. 1. LentiMark, LEAG, and FDP

were developed and introduced to address problems 1 to 3, respectively.

The LEAG is a type of moiré pattern created with lenticular lenses and precise stripe patterns, where the position of black lines changes depending on the viewing angle (Fig. 2). By analyzing the LEAG, high-accuracy orientation information around the marker's two axes can be obtained. Using this information for orientation estimation allows for high-accuracy orientation measurement [20][24][25][26] with errors of about $0.5^\circ$ even from the front direction of the marker (solving problem 1)).

The FDP has a structure similar to a washboard, with small triangular prisms arranged in rows. By painting each side in black and white, it exhibits the behavior shown in Fig. 3. Analyzing the FDP helps determine the general orientation of the marker (up, down, left, or right), enabling the detection of orientation inversion caused by pose ambiguity. If inversion is detected, the initial estimate is corrected to ensure the correct orientation [23], thus solving problem 2).

The feature dots serve as feature points on the marker, replacing the vertices of traditional markers. While the apparent position of the vertices is susceptible to focal blur and variations in lighting intensity, the central positions of the feature dots are less affected by these factors and can be

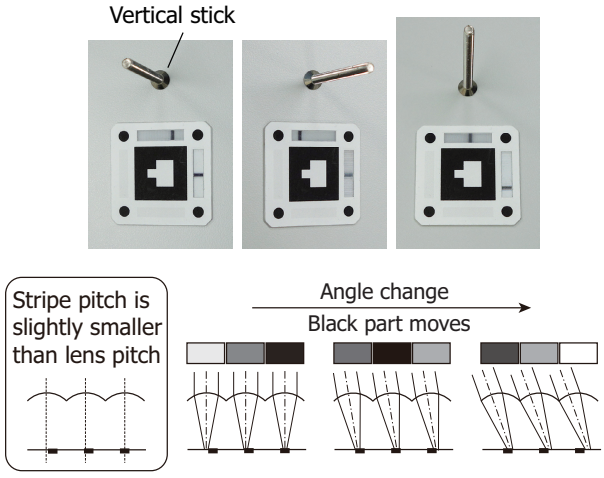


Fig. 2. (Top) LEAG behavior. (Bottom) Principle of LEAG pattern change.

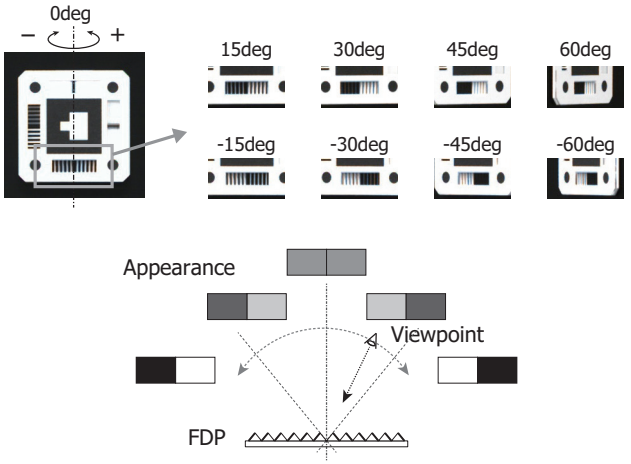


Fig. 3. (Top) FDP behavior. (Bottom) Principle of FDP pattern change.

detected more stably [22]. This enables a more accurate capture of changes in the marker's pose, significantly improving problem 3). The depth direction position estimation error has been reduced to 0.1% of the observation distance.

The LEAG is an optical component that generates moiré patterns, which appear to move depending on the viewing angle, using a single stripe pattern and a lenticular lens instead of two stripe patterns. Therefore, the technology of LentiMark can be considered a fusion of both approaches described in II-A and II-B. The advantage of this method is that the pattern can be observed using inexpensive, commonly available cameras, such as standard webcams, without the need for active lighting. Additionally, the changes in the pattern are easy for humans to understand. In fact, leveraging this latter characteristic, a device for visually measuring vertical orientation has also been developed [33].

These advantages can also be claimed for the FDP. However, both the LEAG and FDP require specialized precision manufacturing techniques, making them difficult for the average person to produce on their own. This is believed to lead to the increased manufacturing cost of LentiMark and hinder its widespread adoption.

To address this issue, we developed a method to create optical components with functions similar to those of the LEAG and FDP using transparent cylinders. This will be detailed in the following sections.

## III. Pose Visualization Using Transparent Cylinders

### A. How to Make New LEAG and FDP

The transparent cylinder functions as a kind of lens, and its optical properties remain constant regardless of the angle around the cylinder axis. Utilizing this characteristic, the author discovered that LEAG and FDP can be created by combining it with a simple black-and-white pattern, as shown in Fig. 4. They were named c-LEAG (cylindrical LEAG) and c-FDP (cylindrical FDP), respectively. The transparent cylinder is made from an acrylic rod. The black-and-white

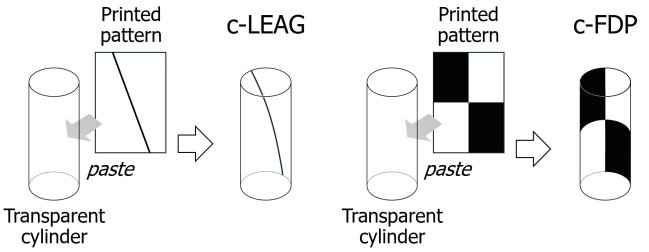


Fig. 4. How to make LEAG (left) and FDP (right) using transparent cylinder.

pattern is printed on regular paper using an inkjet printer and attached to the cylinder using highly transparent double-sided adhesive tape or a similar method. All materials are commonly available, and no special equipment is required for assembly. Therefore, both c-LEAG and c-FDP can be easily self-made by anyone.

### B. Principle of c-LEAG and c-FDP

Fig. 5 shows the mechanism of pattern generation in the c-LEAG. The transparent cylinder has the function of magnifying the image on the back side of a certain-width area parallel to the cylinder axis in a direction perpendicular to the line of sight and the cylinder axis. Therefore, when the back image consists of a diagonal line, the line appears to move along the cylinder axis with a smaller tilt and thicker width as the viewing direction changes. Since the position of the diagonal line on the cylinder axis corresponds to the viewing direction after magnification, it is possible to determine the viewing direction by knowing the position of the appeared diagonal line.

Fig. 6 shows the mechanism of pattern generation in the c-FDP. c-FDP is also created based on a similar principle as c-LEAG. The back image uses a minimum unit of a black-and-white checkerboard pattern, so, like the previous FDP, the positions of white and black reverse depending on the viewing angle. By observing this pattern, it is possible to determine the general orientation of the marker, such as whether it is facing right or left, or up or down. Although a pattern with mixed white and black is seen when viewing c-FDP from the front, this does not pose a problem because, when viewed from the front, the orientation information is obtained solely from c-LEAG, not from c-FDP.

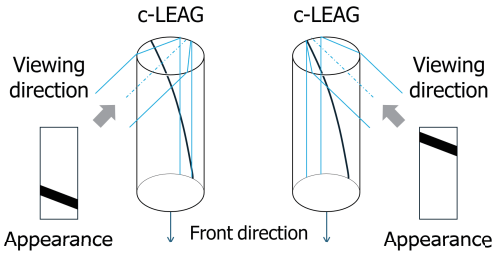


Fig. 5. Mechanism of pattern generation in c-LEAG.

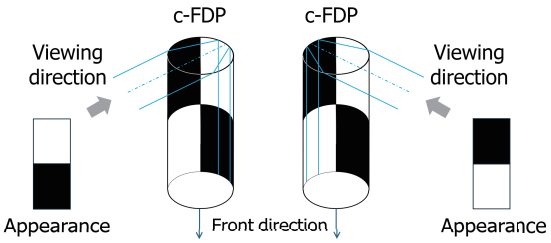


Fig. 6. Mechanism of pattern generation in c-FDP.

TABLE I lists the utilization angle range and the information obtained for c-LEAG and c-FDP. Similar to the previous LEAG and FDP, they are used complementarily according to their respective purposes.

### C. c-LEAG and c-FDP Prototypes

*1) Appearance, Dimensions, and Pattern Design:* Fig. 7 presents images of the fabricated c-LEAG and c-FDP, alongside diagrams of the black-and-white patterns attached to each. The printed patterns cover half of the cylinder's circumference.

We used cylindrical acrylic rods with a diameter of 6 mm (radius $r$=3 mm) and cut them to a length of $l$=24 mm. The slanted pattern for the c-LEAG is designed so that a 60° change in the viewing angle causes the center of the enlarged line to shift by a distance of $l$.

*2) Reduction of Reflected Light:* The surface of the acrylic cylinder tends to reflect light, which can sometimes cause reflections to overlap with the c-LEAG or c-FDP patterns, interfering with accurate measurements. To mitigate this issue, we needed a manually implementable method to reduce surface reflection. We experimented with wrapping the cylinder in mending tape and low-reflection film. However, these approaches obscured the patterns, and due to the lack of flexibility and inadequate adhesion of the sheets, it was difficult to process and maintain performance, ultimately leading to unsatisfactory results.

In contrast, the simplest and most effective solution was to lightly frost the surface by sanding it with superfine (1500-grit) waterproof sandpaper. This sandpaper is also commonly available. Fig. 8 shows a visual comparison between an untreated transparent cylinder and a sanded transparent cylinder. Fig. 8(a) compares their appearance, (b) compares the transparency of the rear patterns, and (c) compares the reflection of light on the cylinder's surface. As demonstrated,

TABLE I
UTILIZATION ANGLE RANGE AND INFORMATION OBTAINED.

| | Utilization Angle Range (Front direction is 0°) | Information Obtained |
|---|---|---|
| c-LEAG | −15° – +15° | Position on the straight line (continuous value) |
| c-FDP | −65° – −15°, +15° – +65° | Positional relationship between black and white (binary) |

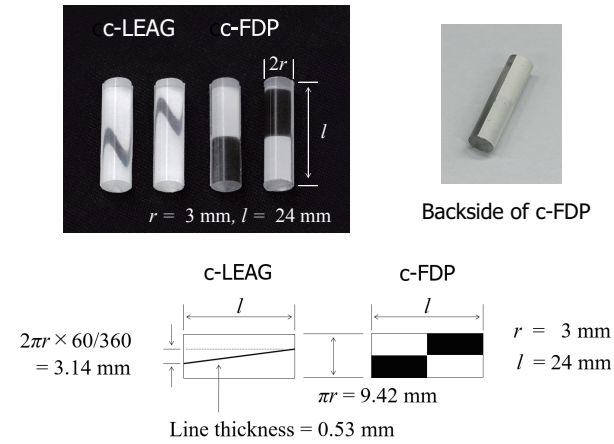


Fig. 7. c-LEAG and c-FDP prototypes and black and white pattern diagrams.

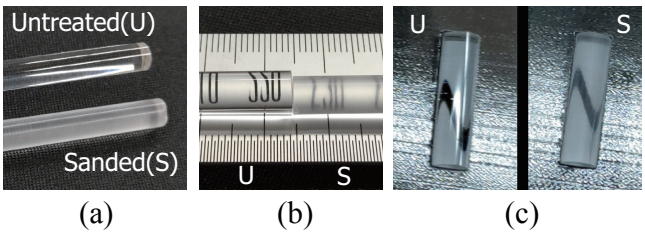


Fig. 8. Comparison between untreated and sanded transparent cylinders: (a) appearance, (b) transparency of rear patterns, and (c) reflection of light on the cylinder surface. The sanded surface reduces light reflection while maintaining clear visibility of the patterns.

by applying moderate sanding, we were able to reduce light reflection while still clearly visualizing the c-LEAG and c-FDP patterns.

*3) Line Thickness of c-LEAG:* Empirically, from the perspective of image processing, the thickness $w$ of the enlarged lines along the c-LEAG axis should ideally be about 1/7 (14.3%) to 1/6 (16.7%) of the length $l$ of the axis. Fig. 9 illustrates the differences in the thickness of the enlarged lines when varying the thickness of the printed lines. This result indicates that for the current prototype, printing the oblique lines for c-LEAG with a thickness of 1.5 pt is just right. It is also important to note that even when lines are printed with the same thickness, the value of $w$ may change depending on the angle of inclination.

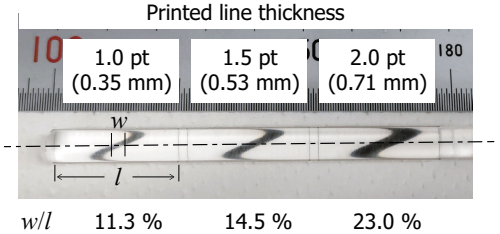


Fig. 9. Comparison of enlarged line thickness influenced by rear pattern line thickness.

### D. Optical Analysis of c-LEAG and c-FDP

This section describes the optical analysis of the behavior of c-LEAG and c-FDP. First, terms that will be frequently used in the following explanations are defined, followed by the presentation of the analysis results of c-LEAG and c-FDP in that order.

*1) Visual-line Angle and Black Point:* Fig. 10 shows the definition of visual-line angles $\varphi$, $\theta_1$, and the Black Point (BP). The cylinder represents c-LEAG or c-FDP. As described later, half of the cylinders of c-LEAG and c-FDP are embedded in the marker with printed patterns, while the other half extends above the marker's surface. The plane passing through both the cylinder axis and the viewpoint is defined as the ray-tracing plane. All analyses and observations will focus solely on phenomena occurring within this plane.

The angle between the normal to the marker surface and the ray-tracing plane is referred to as the visual-line angle $\varphi$. This concept is common to both c-LEAG and c-FDP. On the other hand, a concept unique to c-LEAG is the Black Point (BP). The BP refers to the intersection between the cylinder axis and the centerline of the enlarged black line. The angle between the line connecting the viewpoint and the BP, and the line perpendicular to the axis, is defined as the visual-line angle $\theta_1$.

*2) Optical Analysis of c-LEAG:* The c-LEAG is a component that provides visual-line angle information based on the position of the BP. In order to utilize the function of the c-LEAG, we analyzed the relationship between the BP position, denoted as $p$, and the visual-line angles $\varphi$ and $\theta_1$ using Fig. 11.

Let $n_1$ and $n_2$ represent the refractive indices of air and acrylic, respectively, and let $\theta_1$ and $\theta_2$ represent the angles of incidence and refraction, respectively. According to the well-known Snell's law, (1) holds.

$$\frac{n_1}{n_2} = \frac{\sin\theta_2}{\sin\theta_1} \tag{1}$$

Fig. 11(2) is a development view of half of the cylindrical surface on the marker side. Let $Q$ be the intersection point between the ray-tracing plane $S$ and the printed diagonal line,

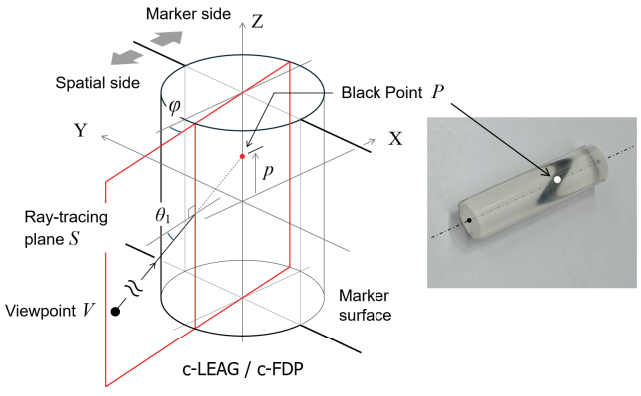


Fig. 10. Definition of visual-line angles $\varphi$, $\theta_1$, and Black Point (BP).

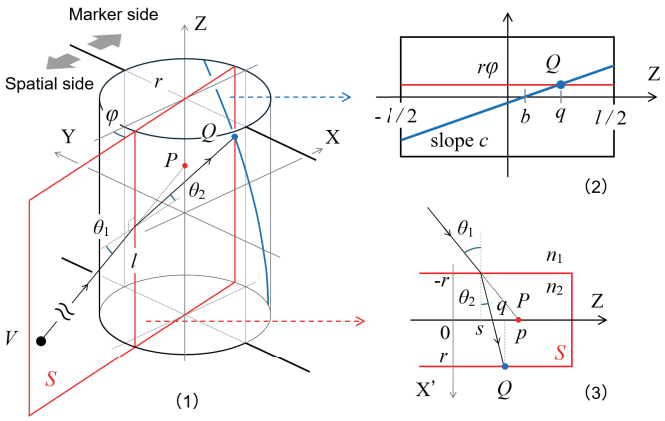


Fig. 11. Optical analysis of c-LEAG.

and let $q$ be its position along the axis. From Fig. 11(2), (2) holds.

$$q = cr\varphi + b \tag{2}$$

Additionally, Fig. 11(3) illustrates the refraction of the light ray in the ray-tracing plane and defines each parameter. From this figure, the following equations (3) and (4) hold.

$$\tan\theta_1 = \frac{p-s}{r} \tag{3}$$

$$\tan\theta_2 = \frac{q-s}{2r} \tag{4}$$

By solving (1) through (4), the relationship between the visual-line angles $\varphi$ and $\theta_1$, and the BP position $p$ is obtained as follows. Here, $c$, $n_1$, $n_2$, $r$, and $b$ are constants.

$$\varphi = \frac{1}{c}\left(2\tan\left(\sin^{-1}\left(\frac{n_1}{n_2}\sin\theta_1\right)\right) - \tan\theta_1 + \frac{1}{r}(p-b)\right) \tag{5}$$

*3) Viewpoint Plane:* An example of the plot showing the relationship between $\varphi$ and $\theta_1$ using (5) is presented in Fig. 12. Here, $c = l/(60\times\pi/180)$, $n_1 = 1.0$, $n_2 = 1.49$ (acrylic), $r = 0.003$, $b = 0$ are used, and three cases of $p = -0.012$, 0.0, 0.006 are shown.

In all cases, the interval of $\theta_1$ from -15° to 15° can be approximated by a straight line with a slope of 23.094, and the maximum error (distance from the approximate line) is about 0.3° in $\theta_1$. Furthermore, for a given BP position $p$, when the positions of viewpoints satisfying (5) are plotted in space, those with $\theta_1$ in the range of -15° to 15° lie approximately on a plane whose normal vector $\boldsymbol{v}_{S_v}$ is

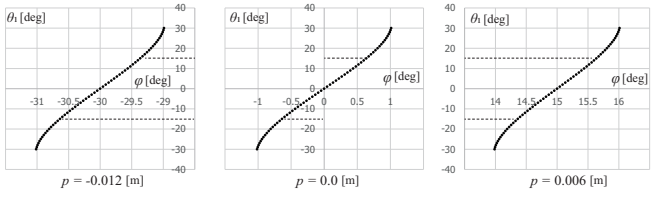


Fig. 12. Relationship between $\varphi$ and $\theta_1$.

$$\boldsymbol{v}_{S_v} = (\sin\varphi_0/\sqrt{1-z_d^2},\ -\cos\varphi_0/\sqrt{1-z_d^2},\ z_d). \quad (6)$$

Here, $\varphi_0$ denotes the value of $\varphi$ at $\theta_1 = 0$ for each $p$. Furthermore, simulation results indicate that, under the same conditions, $z_d$ is approximately 0.041. This plane is defined as the viewpoint plane $S_v$ as shown in Fig. 13.

*4) Optical Analysis of c-FDP:* Using the ray-tracing model of the c-FDP shown in Fig. 14 (left), the range of viewing angles in which the white and black regions of the c-FDP are clearly separated was investigated. By means of a geometrical calculation similar to that used in the optical analysis of the c-LEAG, it is possible to determine the position on the rear side where a light ray incident on the c-FDP strikes. Fig. 14 (right) shows the relationship between $c$ and $\varphi$ obtained from this calculation.

From this result, it is found that the range magnified by the c-FDP is $-12^\circ < \varphi < 12^\circ$. When the viewing angle with respect to the c-FDP is less than $-12^\circ$ or greater than $12^\circ$, the white and black regions appear clearly separated without any mixture. Outside this range, in the frontal direction, a checkerboard pattern in which white and black are intermixed can be seen. However, since the c-LEAG can still be observed within this angular range, enabling pose correction and pose-inversion detection,there is no need for the c-FDP to be observed.

## IV. Fiducial Marker using Transparent Cylinders

In this section, we describe a high-accuracy fiducial marker, which can be self-fabricated using two c-LEAGs and two c-FDPs, as well as its measurement algorithm. The newly developed high-accuracy marker in this study is referred to as c-LentiMark, since it is a LentiMark-type marker that employs cylindrical lenses.

### A. Design and Structure of c-LentiMark

Fig. 15 shows the c-LentiMark and its structure. The c-LentiMark is a design in which the LEAG and FDP of the original LentiMark (Fig. 1) are replaced by a c-LEAG and a c-FDP, respectively. However, the distances between the

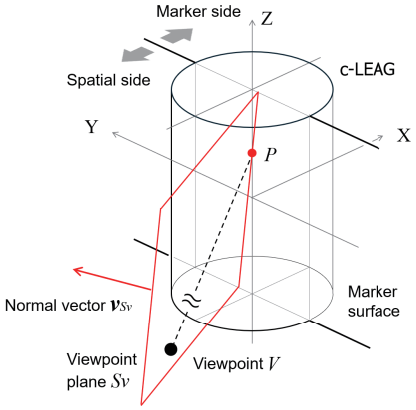


Fig. 13. Viewpoint plane.

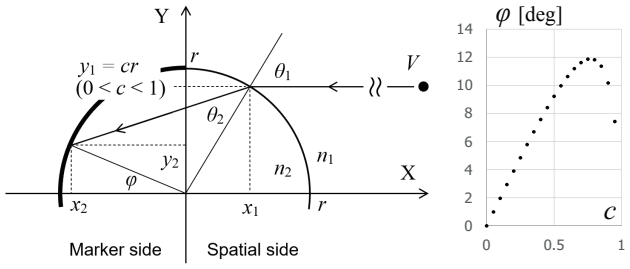


Fig. 14. Ray-tracing model of the c-FDP (left) and the relationship between $c$ and $\varphi$ (right).

elements that constitute the marker are made larger in the c-LentiMark. This is because both the c-LEAG and the c-FDP protrude 3 mm above the marker plane, and if their distances from the 2D code or feature dots are too short, they may obscure these elements when viewed from an oblique angle.

As the substrate of the marker, two styrene boards with a thickness of 3 mm were stacked. Holes were made in the front board, into which the c-LEAGs and c-FDPs were inserted and fixed. The feature dots and 2D code were printed on matte paper using an inkjet printer and affixed to the surface with double-sided adhesive tape. These materials are generally available and easy to process. Therefore, the c-LentiMark can be readily self-fabricated. If a 3D printer is available, fabricating the marker substrate using a 3D printer is also a practical approach. An example of a prototype is shown in Fig. 16.

### B. Measurement Algorithm of c-LentiMark

The measurement algorithm of the c-LentiMark is basically the same as that of the LentiMark with FDP [23]. However, it should be noted that for both the c-LEAG and the c-FDP, the axes responsible for pose correction and pose-inversion detection differ from those in the previous LentiMark. For example, the c-LEAG located at the position where a LEAG visualizing the pose around the x-axis was placed is now configured to visualize the pose around the y-axis.

The outline of the algorithm is as follows:

1) Detect the 2D code and the four surrounding feature dots.

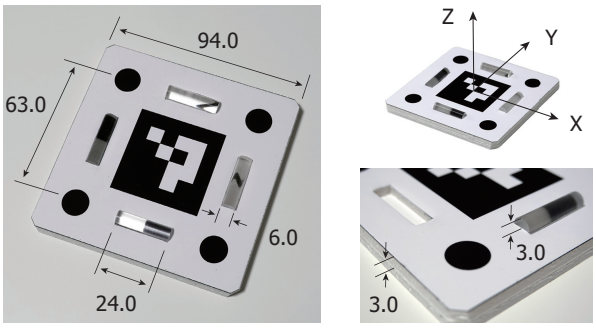


Fig. 15. c-LentiMark (left), definition of the coordinate system (top right), and structure (bottom right). Dimensions in mm.

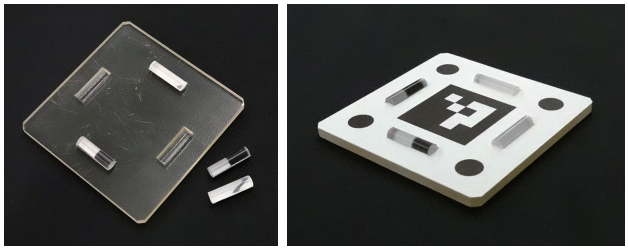

Fig. 16. c-LentiMark fabrication with a 3D printer.

2) Estimate the initial pose of the marker based on the positions of the feature dots in the image.
3) When the viewing angle with respect to the marker normal falls within the range shown in the lower row of TABLE I, observe the two c-FDPs, and if pose inversion is detected, correct the initial pose.
4) When the viewing angle with respect to the marker normal falls within the range shown in the upper row of TABLE I, observe the two c-LEAGs, and correct the pose primarily using the two viewpoint planes derived from the BP values.

## V. Performance Evaluation of c-LentiMark

This section presents the evaluation of the effectiveness and performance of c-LentiMark.

### A. Measurement Environment

Fig. 17 shows the measurement environment. The c-LentiMark test piece was mounted on a two-axis rotation stage, and a Grasshopper3 (GS3-U3-23S6M-C, FLIR Systems, Inc.) USB3.0 CMOS monochrome camera (1280 × 720 pixels, FOV 33.7° × 19.3°) was used as the vision sensor. The camera, mounted on a linear slider, could be positioned 400–1500 mm from the marker. Processing was performed on a laptop (64-bit CPU, 2.11 GHz, 16 GB RAM) at 25 FPS, using C/C++ and OpenCV 3.4.

The camera and marker coordinate systems were defined as in Fig. 17. The marker orientation was adjusted by rotating $a_Y$ [deg] about the Y axis and then $a_Z$ [deg] about the Z axis, with the resulting attitude expressed as ($a_Y$, $a_Z$).

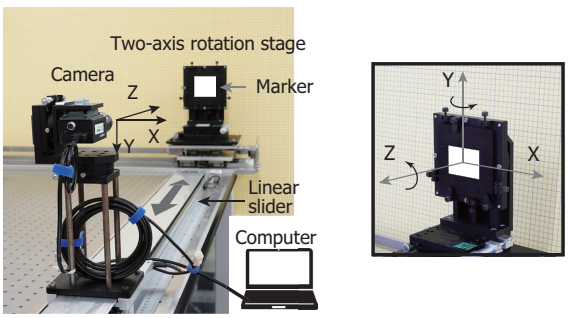


Fig. 17. Measurement environment.

*1) Verification of Measurable Orientation Range:* The measurable orientation ranges of the c-LEAG and c-FDP placed on the marker's x-axis, as well as of the c-LentiMark, were investigated. Here, with $a_Z = 0$, the measurable range of $a_Y$ was examined. The observation distance was 1000 mm. The results are summarized in Table II.

The asymmetry of the results with respect to zero is considered to arise from factors such as the offset of the central positions when installing the c-LEAGs and c-FDPs, and the slight difference between $a_Y$ and the visual line angle defined in Section III-D. However, these effects are not problematic in practical use.

From this verification, it was confirmed that the c-LEAG and c-FDP are available within the pose ranges defined in Table I. It was also confirmed that, within these ranges, neither the c-LEAG nor the c-FDP obstructs the recognition of the 2D code or the feature dots.

*2) Improvement of Orientation Estimation Accuracy with c-LEAG:* We compared the orientation estimation accuracy with and without the use of c-LEAG. The orientation estimation error was defined as the angular difference between the ground-truth and estimated values for each axis of the marker coordinate system (Fig. 18, left). The parameter was set to $a_Z = 0$, and orientation estimation was performed while varying $a_Y$. The observation distance was 1428 mm. The results are shown in Fig. 18 (right). The error became particularly large when the marker was observed from the frontal direction; however, by applying pose correction using the information provided by c-LEAG, high-accuracy orientation estimation was achieved. The maximum orientation error was reduced to approximately 0.4° when using c-LEAG-based pose correction, even in near-frontal observations. These results demonstrate the effectiveness of c-LEAG as well as the validity of the optical analysis of c-LEAG and the measurement algorithm of c-LentiMark.

TABLE II
Measurable Orientation Range.

| | Measurable Angle Range ($a_Y$) |
|---|---|
| c-LEAG | −24.8° – +19.7° |
| c-FDP | −68.4° – −2.4°, +8.5° – +71.5° |
| c-LentiMark | −74.1° – +74.3° |

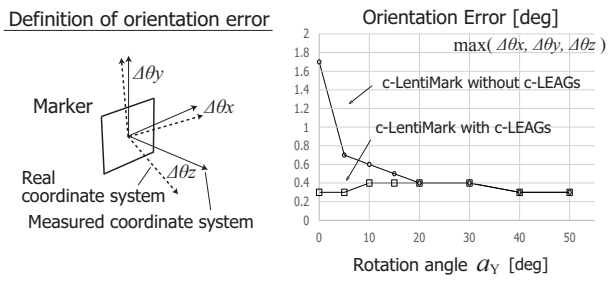


Fig. 18. Orientation measurement error. Distance: 1428 mm, Orientation:($a_Y$,0.0).

*3) Verification of c-FDP Detection Performance:* During the orientation estimation accuracy measurements described above, observations of c-FDP were conducted simultaneously. As a result, no false detections occurred (i.e., no cases were found in which the positions of black and white were incorrectly judged in reverse). This demonstrates that c-FDP measurements can be performed correctly over a wide angular range. Although pose inversion due to pose ambiguity did not occur in the present experimental environment, the pose inversion correction algorithm for c-LentiMark is identical to the one whose effectiveness has already been confirmed in [23]. Therefore, we consider that pose inversion can also be reliably handled without difficulty.

## VI. Concluding Remarks

In this study, we proposed a novel method for extracting orientation information using transparent cylinders, and by applying this method, we developed a groundbreaking high-accuracy fiducial marker that achieves measurement accuracy comparable to conventional high-accuracy markers. The most notable feature of this marker is that it can be self-fabricated using generally available materials. Future work will focus on more comprehensive performance evaluations and considerations for releasing the marker measurement software.

## References


[1] J. Rekimoto, Matrix: A realtime object identification and registration method for augmented reality, in Proc. IEEE 3rd Asia Pacific Computer Human Interaction, 1998, pp. 63–68.

[2] H. M. Balanji, A. E. Turgut, and L. T. Tunc, A novel vision-based calibration framework for industrial robotic manipulators, Robotics and Computer-Integrated Manufacturing, vol. 73, 102248, 2022.

[3] Y. Yin, et al., Vision-Based Autonomous Robots Calibration for Large-size Workspace Using ArUco Map and Single Camera Systems. Precision Engineering, vol. 90, pp. 191–204, 2024.

[4] Y. Zheng, et al., Fiducial Marker Based Patient-to-Robot Registration and Target Tracking for Automatic Extra-body Ultrasound Imaging, in Proc. IEEE Int.l Conf. Automation Science and Engineering (CASE), IEEE Xplore, 2024.

[5] M. Yang, and E. Yang, Two-stage multi-sensor fusion positioning system with seamless switching for cooperative mobile robot and manipulator system, Int. Journal of Intelligent Robotics and Applications, vol. 7, no. 2, pp. 275–290, 2023.

[6] R. Adámek, et al., Analytical Models for Pose Estimate Variance of Planar Fiducial Markers for Mobile Robot Localisation, Sensors, 23.12: 5746, 2023.

[7] W. Zhang, et al., Precise visual positioning of agricultural mobile robots with a fiducial marker reprojection approach, Measurement Science and Technology, 34.11: 115110, 2023.

[8] F. Wang, et al., UAV navigation in large-scale GPS-denied bridge environments using fiducial marker-corrected stereo visual-inertial localisation, Automation in Construction, 156: 105139, 2023.

[9] A. Waqas, D. Kang, and Y. Cha, Deep learning-based obstacle-avoiding autonomous UAVs with fiducial marker-based localization for structural health monitoring, Structural Health Monitoring, vol. 23, no. 2, pp. 971-990, 2024.

[10] D. Amodei, et al., Concrete problems in AI safety, arXiv preprint arXiv:1606.06565, 2016.

[11] A. Bajcsy, and J. F. Fisac, Human-AI Safety: A Descendant of Generative AI and Control Systems Safety, arXiv preprint arXiv:2405.09794, 2024.

[12] ARToolKit developer homepage, http://artoolkit.sourceforge.net/

[13] F. Bergamasco, A. Albarelli, E. Rodolà and A. Torsello, RUNE-Tag: A high accuracy fiducial marker with strong occlusion resilience, in Proc. IEEE Conf. Computer Vision and Pattern Recognition (CVPR), 2011, pp. 113–120.

[14] J. Wang and E. Olson, AprilTag 2: Efficient and robust fiducial detection, in Proc. 2016 IEEE/RSJ Int. Conf. Intelligent Robots and Systems (IROS), 2016, pp. 4193–4198.

[15] J. DeGol, T. Bretl, and D. Hoiem, ChromaTag: A Colored Marker and Fast Detection Algorithm, in Proc. The IEEE Int. Conf. Computer Vision (ICCV), 2017, pp. 1472–1481.

[16] F. J. Romero-Ramirez, R. Muñoz-Salinas, R. Medina-Carnicer, Speeded up detection of squared fiducial markers, Image and Vision Computing, vol. 76, pp. 38–47, 2018.

[17] V. Lepetit, F. Moreno-Noguer, and P. Fua, EPnP: An accurate O(n) solution to the PnP problem, Int. Journal of Computer Vision, vol. 81(2), pp. 155–166, 2009.

[18] G. Terzakis, and M. Lourakis, A consistently fast and globally optimal solution to the perspective-n-point problem, in Proc. European Conference on Computer Vision (ECCV), 2020, pp. 478–494.

[19] D. Abawi, J. Bienwald, and R. Dörner, Accuracy in Optical Tracking with Fiducial Markers:An Accuracy Function for ARToolKit, in Proc. the Third IEEE and ACM Int. Symp. Mixed and Augmented Reality (ISMAR), 2004, pp. 260–261.

[20] H. Tanaka, Y. Sumi, and Y. Matsumoto, A Visual Marker for Precise Pose Estimation based on Lenticular Lenses, in Proc. 2012 IEEE Int. Conf. Robotics and Automation (ICRA), 2012, pp. 5222–5227.

[21] H. Tanaka, Y. Sumi, and Y. Matsumoto, A high-accuracy visual marker based on a microlens array, in Proc. 2012 IEEE/RSJ Int. Conf. Intelligent Robots and Systems (IROS), 2012. pp. 4192–4197.

[22] H. Tanaka, K. Ogata, and Y. Matsumoto, Improving the accuracy of visual markers by four dots and image interpolation, in Proc. 2016 IEEE Int.l Symp. Robotics and Intelligent Sensors (IRIS), 2016. pp. 178–183.

[23] H. Tanaka, K. Ogata, and Y. Matsumoto, Solving pose ambiguity of planar visual marker by wavelike two-tone patterns, in Proc 2017 IEEE/RSJ Int. Conf. Intelligent Robots and Systems (IROS), 2017, pp. 568–573.

[24] H. Tanaka, Ultra-High-Accuracy Visual Marker for Indoor Precise Positioning, in Proc. 2020 IEEE Int. Conf. Robotics and Automation (ICRA), 2020, pp. 2338–2343.

[25] H. Tanaka, and K. Ogata, A High-Accuracy Fiducial Marker with Parallel Lenticular Angle Gauges, in Proc. 2021 IEEE/RSJ Int. Conf. Intelligent Robots and Systems (IROS), 2021, pp. 8091–8096.

[26] H. Tanaka, and K. Ogata, LeagTag: An Elongated High-Accuracy Fiducial Marker for Tight Spaces, in Proc.2024 IEEE Int. Conf. Robotics and Automation (ICRA), 2024, pp. 17438–17444.

[27] B. Armstrong, et al., RGR-3D: simple, cheap detection of 6-DOF pose for teleoperation, and robot programming and calibration, in Proc. 2002 IEEE Int. Conf. Robotics and Automation (ICRA), 2002, vol.3, pp. 2938–2943.

[28] M. Eschelbach, et al., Comparison of prospective head motion correction with NMR field probes and an optical tracking system, Magnetic resonance in medicine, 81.1: pp. 719–729, 2019.

[29] S. Qiu, H. Amata, and W. Heidrich, Moirétag: Angular measurement and tracking with a passive marker, In Proc.ACM SIGGRAPH 2023, 2023. pp. 1–10.

[30] A. Mohan, et al., Bokode: imperceptible visual tags for camera based interaction from a distance, in Proc. ACM SIGGRAPH 2009 papers. 2009, pp. 1–8.

[31] I. Schillebeeckx, et al., The geometry of colorful, lenticular fiducial markers, in Proc. 2015 IEEE Int. Conf. 3D Vision, 2015 pp. 487–499.

[32] I. Schillebeeckx, R. Pless, Pose hashing with microlens arrays, in Proc. The 14th European Conf. Computer Vision (ECCV) , Part III 14, 2016, pp. 600–614.

[33] H. Tanaka, A Perpendicular Direction Gauge Using a Lenticular Lens, in Proc. 2021 IEEE/SICE Int. Symp. System Integration (SII), 2021. pp. 827–828.